

## THE ROLE OF MAGNETIC HELICITY IN STRUCTURING THE SOLAR CORONA

K. J. KNIZHNIK<sup>1,2</sup>, S. K. ANTIOCHOS<sup>2</sup>, AND C. R. DEVORE<sup>2</sup>

*Draft version October 9, 2018*

### ABSTRACT

Two of the most widely observed and yet most puzzling features of the Sun's magnetic field are coronal loops that are smooth and laminar and prominences/filaments that are strongly sheared. These two features would seem to be quite unrelated in that the loops are near their minimum-energy current-free state, whereas filaments are regions of high magnetic stress and intense electric currents. We argue that, in fact, these two features are inextricably linked in that both are due to a single process: the injection of magnetic helicity into the corona by photospheric motions and the subsequent evolution of this helicity by coronal reconnection. In this paper, we present numerical simulations of the response of a Parker (1972) corona to photospheric driving motions that have varying degrees of helicity preference. We obtain four main conclusions: 1) in agreement with the helicity condensation model of Antiochos (2013), the inverse cascade of helicity by magnetic reconnection results in the formation of prominences/filaments localized about polarity inversion lines (PILs); 2) this same process removes most structure from the rest of the corona, resulting in smooth and laminar coronal loops; 3) the amount of remnant tangling in coronal loops is inversely dependent on the net helicity injected by the driving motions; and 4) the structure of the solar corona depends only on the helicity preference of the driving motions and not on their detailed time dependence. We discuss the implications of our results for high-resolution observations of the corona.

*Keywords:* Sun: corona – Sun: filaments/prominences – Sun: magnetic fields

### 1. INTRODUCTION

A well-known feature of the solar magnetic field is the observation of filament channels at photospheric polarity inversion lines (PILs). These magnetic structures, situated in the upper chromosphere and lower corona, underlie and support the cool plasma that comprises prominences and filaments (Martin 1998; Gaizauskas 2000). Filament channels are regions of highly sheared magnetic field, containing large amounts of free energy that ultimately is converted into kinetic and thermal energy of the plasma, as well as nonthermal particle energies when filament channels erupt and drive coronal mass ejections (CMEs). The shear inherent in the filament channels is a form of magnetic helicity, and filament channels are known as dextral if they have negative helicity and sinistral if they have positive helicity. Observations indicate that dextral (sinistral) filament channels dominate in the northern (southern) hemisphere (e.g. Martin et al. 1992; Rust & Kumar 1994; Zirker et al. 1997; Pevtsov et al. 2003). This hemispheric helicity rule has also been observed in quiet-Sun magnetic fields (Pevtsov & Longcope 2001), sigmoids (Rust & Kumar 1996), active-region magnetic fields (Seehafer 1990), coronal mass ejections (CMEs), and sunspot whorls (Pevtsov et al. 2014). The strength of the preference ranges from about 55% in active-region filaments (Martin 1994), to over 80% in quiescent filaments (Pevtsov et al. 2003) and does not seem to change with solar cycle (Hale 1927; Martin 1994; Hagino & Sakurai 2002).

A second, seemingly unrelated, feature of the solar magnetic field is the observation of loops in the closed-

field corona that appear to be near their minimum energy, current-free state. These loops have been observed at high resolution in *Transition Region and Coronal Explorer (TRACE)* XUV and X-ray images, such as the one in Figure 1, where they are seen to be very smooth and laminar, with little to no tangling (Schrijver et al. 1999). In other words, there appears to be very little magnetic helicity associated with the topology of these loops. The picture of the corona that emerges, therefore, is one in which magnetic helicity manifests itself at specific locations, namely above PILs, while leaving the rest of the corona generally smooth and quasi-potential.

Since the corona has very high Lundquist number, its magnetic helicity is believed to originate by injection from the photosphere, either by flux emergence or footpoint motions after emergence, and to be lost to the heliosphere by flux opening in CMEs and streamer blowouts. *Solar Dynamics Observatory (SDO)* measurements of helicity injection into the coronal field indicate that shearing and twisting motions by the photosphere dominate the flux emergence (Liu & Schuck 2012), meaning that the helicity budget of the corona is primarily due to the jostling of existing flux at the surface, rather than due to new flux emerging into the corona. Observations of photospheric convection show that these footpoint motions are highly complex (Schmieder et al. 2014), with convective cells appearing randomly throughout the photosphere, and occur over a broad range of scales, of order minutes for granules and days for supergranules (Hirzberger et al. 2008). From the standpoint of helicity injection, however, the important flows are those that twist the field. Compression of the field caused by converging flows is not expected to impart any helicity into the field, so these flows cannot be responsible for the shear observed in filament channels. The flows that

<sup>1</sup> Department of Physics and Astronomy, The Johns Hopkins University, Baltimore MD 21287

<sup>2</sup> Heliophysics Science Division, NASA Goddard Space Flight Center, Greenbelt MD 20771

twist up the field, in contrast, do inject a net helicity into the corona. Therefore, we conclude that it is sufficient to model the helicity injection into the corona with simple twisting motions as has been done by many authors (e.g. Wilmot-Smith et al. 2010; Rappazzo et al. 2013). Such flows have routinely been observed in helioseismic measurements (Duvall & Gizon 2000; Gizon & Duvall 2003; Komm et al. 2007; Seligman et al. 2014). Vortical flows on the scale of granules (e.g. Bonet et al. 2008, 2010; Vargas Domínguez et al. 2011, 2015) and supergranules (Brandt et al. 1988; Attie et al. 2009) have also been observed.

These considerations make it very challenging to understand the simultaneous presence in the corona of both filament channels and coronal loops. Magnetic stress is, apparently, injected throughout the solar photosphere, yet is almost nowhere to be found in the corona, except in filament channels. Antiochos (2013) presented a new model for the formation of filament channels, magnetic helicity condensation, based on the well-known inverse cascade of magnetic helicity in turbulent systems. In the helicity condensation model, photospheric convection imparts helicity into the coronal field, and this helicity is then transported throughout the corona by magnetic reconnection, which is well-known to conserve helicity (Woltjer 1958; Taylor 1974, 1986; Berger 1984). Surface convection imparts the same sense of twist to adjacent flux tubes, which are then able to undergo component reconnection at their contact point. This component reconnection produces a single flux tube with an axial flux equal to the sum of the two original axial fluxes, but encircled by the same twist field present on each of the two original flux tubes. In this way the helicity, in the form of twist, inverse-cascades to larger and larger scales. The PIL forms a natural boundary of the flux system, so that when the twist reaches this boundary, it cannot proceed further, since all of the flux has already reconnected. The end result of this process is a mostly axial (untwisted) internal field, and a highly sheared (twisted) field at the PIL, precisely what is observed as a filament channel. At the same time, the untwisted internal field corresponds to the laminar coronal loops. In this way, the helicity condensation model provides a natural mechanism for the simultaneous formation of both highly sheared filament channels and relatively untwisted coronal loops. In this model, these two seemingly unrelated features of the solar atmosphere are actually created by the same process (Antiochos 2013).

The helicity condensation model was initially simulated by Zhao et al. (2015), who injected magnetic helicity into a plane-parallel Parker corona (Parker 1972). These authors found that photospheric motions that inject the same helicity everywhere form filament channels at the PIL. Furthermore, randomizing the photospheric motions while keeping the same helicity injection rate did not qualitatively affect the accumulation of twist flux at the PILs. Zhao et al. (2015) also tested the effect of injecting helicity of opposite signs on adjacent flux tubes, and found that their fields could not reconnect due to the twist components being co-aligned.

In subsequent work (Knizhnik et al. 2015, hereafter KAD15), we rigorously tested the helicity condensation model. We found that it not only qualitatively produced results consistent with the properties of filament chan-

nels, but that the inverse cascade of magnetic helicity due to reconnection produces a twist flux at the PIL that agrees quantitatively with the predictions of the helicity condensation model. Based on this result, we estimated that with the helicity preference observed on the Sun, filament channels will form in about a day or so, in agreement with observations of filament channel formation (Martin 1998; Gaizauskas 2000). We showed that helicity condensation agreed both qualitatively and quantitatively with observed properties of filament channels, and that the process produced relatively untwisted coronal loops everywhere except at the PIL. These results, however, were obtained for a 100% helicity rule, meaning that all of the helicity injected into the corona was of the same sign. An obvious question to be raised is: what happens if a fraction of the injected helicity has the opposite sign? Indeed, this is a more realistic scenario since, as described above, the corona has a hemispheric helicity preference, rather than a rule, so that some helicity of the non-preferred sign is injected into the corona at all times.

It is reasonable to expect that injecting helicity of the opposite sign into the corona would simply slow down the helicity condensation process. However, this result is not as straightforward as it may seem. The simulations of Zhao et al. (2015) demonstrated that adjacent flux tubes have difficulty reconnecting if they are twisted in opposite senses. As a result, the twist was unable to inverse-cascade to larger scales, as is required to form the sheared filament channels and smooth coronal loops. Even if reconnection between the adjacent flux tubes is eventually achieved as a result of some instability – such as ideal kinking – driving the interaction, the twist-flux cancellation is expected to be far from perfect. Substantial residual twist could remain in what otherwise would have been smooth, untwisted coronal loops. Therefore, it is important to test whether sheared filament channels and smooth coronal loops form when both signs of magnetic helicity are injected into the corona.

In this paper, we investigate the effect of varying helicity preference on the structure of the closed-field corona. We performed helicity-conserving numerical simulations that inject helicity into a plane-parallel Parker corona, as we did in KAD15. Extending our previous work, the fraction of helicity of each sign that is injected into the corona was varied. We report on three cases: 1) 100% of the injected helicity is positive; 2) 75%/25% of the injected helicity is positive/negative; and 3) 50%/50% of the injected helicity is positive/negative. To make the simulations as realistic as possible, we also randomized the pattern of helicity injection. We compare the simulations with a fixed pattern of helicity injection to those with a randomized pattern of helicity injection.

The paper is organized as follows. In §2 we discuss the setup and initialization of our numerical simulations. In §3 we describe how magnetic helicity is injected into the domain, and how the helicity preference is employed. In §4 we discuss the results of our simulations, exploring the formation of filament channels and the smoothness of coronal loops for various helicity preferences, and compare the simulations with fixed and randomized patterns of helicity injection. We discuss the implications for understanding coronal magnetic structure in §5.

## 2. NUMERICAL MODEL

The numerical model used in this study was described previously in KAD15. We solve the equations of magnetohydrodynamics (MHD) using the Adaptively Refined Magnetohydrodynamics Solver (ARMS; DeVore & Antiochos 2008) in three Cartesian dimensions. The equations have the form

$$\frac{\partial \rho}{\partial t} + \nabla \cdot \rho \mathbf{v} = 0, \quad (2.1)$$

$$\frac{\partial \rho \mathbf{v}}{\partial t} + \nabla \cdot (\rho \mathbf{v} \mathbf{v}) = -\nabla P + \frac{1}{4\pi} (\nabla \times \mathbf{B}) \times \mathbf{B}, \quad (2.2)$$

$$\frac{\partial T}{\partial t} + \nabla \cdot (T \mathbf{v}) = (2 - \gamma) T \nabla \cdot \mathbf{v}, \quad (2.3)$$

$$\frac{\partial \mathbf{B}}{\partial t} = \nabla \times (\mathbf{v} \times \mathbf{B}). \quad (2.4)$$

Here  $\rho$  is mass density,  $T$  is temperature,  $P$  is thermal pressure,  $\gamma$  is the ratio of specific heats,  $\mathbf{v}$  is velocity,  $\mathbf{B}$  is magnetic field, and  $t$  is time. We close the equations via the ideal gas equation,

$$P = \rho R T, \quad (2.5)$$

where  $R$  is the gas constant.

ARMS uses finite-volume representations of the variables to solve the system of equations. Its Flux Corrected Transport algorithms (DeVore 1991) provide minimal, though finite, numerical dissipation, which allows reconnection to occur. As a result, to a very good approximation, ARMS conserves the magnetic helicity in the system.

We set up a model coronal field that is initially straight and uniform between two plates, as shown in Figure 2. In this model, straight flux tubes represent coronal loops whose apex is located in the center of the domain and with the boundaries representing the photosphere. Our domain size is  $[0, L_x] \times [-L_y, L_y] \times [-L_z, L_z]$ , where  $x$  is taken normal to the photosphere (the vertical direction) and we set  $L_x = 1$ , and  $L_y = L_z = 1.75$ . At all six sides, we use zero-gradient conditions, and the four side walls have open boundary conditions. Closed boundary conditions are employed at the top and bottom, where the magnetic field is line tied at the high- $\beta$  photosphere. The footpoints of the field lines do not move in response to magnetic forces, but do respond to imposed boundary flows to mimic driving at the plasma-dominated photosphere.

As in our previous work, we set the initial, uniform values in our dimensionless simulations to  $\rho_0 = 1$ ,  $T_0 = 1$ ,  $P_0 = 0.05$ , and  $B_0 = \sqrt{4\pi}$ . These choices set the gas constant,  $R = 0.05$ , the Alfvén speed,  $c_{A0} = B_0 / \sqrt{4\pi \rho_0} = 1$ , and the plasma beta,  $\beta_0 = 8\pi P_0 / B_0^2 = 0.1$ .  $\beta \ll 1$  corresponds to a magnetically dominated plasma, which is generally true of the corona. The results discussed below will be given in simulation time, which is normalized to the time required for an Alfvén wave at unit speed ( $c_{A0} = 1$ ) to travel the distance separating the top and bottom plates ( $L_x = 1$ ).

As before, we set up our convective cells in a hexagonal pattern, with 84 cells on the top and bottom plates. Each individual cell has the same spatial and temporal profiles

described in KAD15. The angular velocity of each cell is given by

$$\Omega(r, t) = \begin{cases} -\Omega_0 g(r) f(t) & \text{if } r \leq a_0 \\ 0 & \text{if } r > a_0 \end{cases} \quad (2.6)$$

where

$$g(r) = \left(\frac{r}{a_0}\right)^4 - \left(\frac{r}{a_0}\right)^8 \quad (2.7)$$

and

$$f(t) = \frac{1}{2} \left[ 1 - \cos\left(\frac{2\pi t}{\tau}\right) \right] \quad (2.8)$$

with  $\Omega_0 = 7.5$  and  $r$  the cylindrical radial coordinate with respect to the center of the convective cell. The flow is confined to a circle of radius  $a_0 = 0.125$ , and the magnitude of the flow is ramped up and back down over a period  $\tau = 3.35$ . As demonstrated in KAD15, this velocity profile for the convective cells conserves the normal magnetic field distribution,  $\mathbf{B}_x$ , on the photospheric boundaries.

The simulation mesh for this study is specified, as in KAD15, such that we resolve very finely that part of the domain where these photospheric flows are imposed and the coronal magnetic field is influenced by the surface stresses. We use  $4 \times 14 \times 14$  elemental blocks to span the simulation domain, each containing  $8 \times 8 \times 8$  uniform, cubic grid cells. In the highly resolved portion of our simulation volume, which included the convective cells, the lanes between them, the untwisted region in the interior, and a buffer region around the outer perimeter of the pattern, we applied two additional levels of refinement, such that each rotation was covered by 32 grid points across its diameter. Closer to the side walls, the grid was allowed to coarsen by two levels, such that the grid spacing near the walls was a factor of four larger than in the interior. With this grid distribution, the ratio of the smallest grid spacing to the height of the box was about 0.001, resulting in a magnetic Reynolds number  $R_m \sim 10^3$ .

The key difference from our previous work, described in detail below, is that the sense of rotation of each cell, as well as the angular orientation of the entire pattern of cells, is changed randomly during the course of the simulations. The top plate mirrors the bottom plate at all times. These variations are meant to model more faithfully the random nature of the Sun's surface convection. Below, we describe how the relative fraction of cells rotating in the opposite sense affects the amount of magnetic helicity injected into our simulations.

## 3. MAGNETIC HELICITY INJECTION

Magnetic helicity is a topological quantity describing linkages in the magnetic field, such as twist, shear, and writhe. In a volume  $V$  bounded by a surface  $S$ , which need not be a magnetic flux surface, the relative magnetic helicity is given by (Finn & Antonsen 1985)

$$H = \int_V (\mathbf{A} + \mathbf{A}_P) \cdot (\mathbf{B} - \mathbf{B}_P) dV. \quad (3.1)$$

Here  $\mathbf{B} = \nabla \times \mathbf{A}$  is the magnetic field in the volume  $V$ , generated by the vector potential  $\mathbf{A}$ , and  $\mathbf{B}_P = \nabla \times \mathbf{A}_P$  is a current-free field ( $\nabla \times \mathbf{B}_P = 0$ ) satisfying  $\mathbf{B}_P \cdot \hat{\mathbf{n}}|_S =$

$\mathbf{B} \cdot \hat{\mathbf{n}}|_S$ . The rate of change of the helicity in Equation (3.1) is given in ideal MHD by

$$\frac{dH}{dt} = 2 \oint_S \left[ (\mathbf{A}_P \cdot \mathbf{v}) \mathbf{B} - (\mathbf{A}_P \cdot \mathbf{B}) \mathbf{v} \right] \cdot d\mathbf{S}. \quad (3.2)$$

The first term represents the effects of motions on the boundary with velocity  $\mathbf{v}$ , while the second term represents the emergence or submergence of magnetic field through the boundary. As a result, the magnetic helicity in our simulation changes only due to motions on or through the boundary. In highly conducting ( $R_m \gg 1$ ) plasmas, such as the corona, magnetic helicity is conserved even in the presence of a small localized resistivity that enables magnetic reconnection (Woltjer 1958; Taylor 1974, 1986; Berger 1984). Since no new flux is being injected at our top and bottom boundaries, and the side boundaries are sufficiently far away that no flux leaves the system, the rate of change of magnetic helicity in our simulation reduces to

$$\frac{dH}{dt} = 2 \oint_S (\mathbf{A}_P \cdot \mathbf{v}) \mathbf{B} \cdot d\mathbf{S}. \quad (3.3)$$

The magnetic helicity  $H_0$  injected into a single flux tube (i.e. one top/bottom pair of rotation cells) over one cycle is obtained by integrating Equation 3.3 from  $t = 0$  to  $t = \tau$ , employing Equations 2.6–2.8 and the vector potential for the uniform, current-free initial field,

$$\mathbf{A}_P = \frac{B_0}{2} (y\hat{\mathbf{z}} - z\hat{\mathbf{y}}). \quad (3.4)$$

If the sense of rotation is clockwise, the resulting positive helicity injected is

$$H_0 = 2 \times 10^{-2}. \quad (3.5)$$

Trivially, the net helicity  $H_\Sigma$  injected into  $N$  such flux tubes all twisted in the clockwise sense, as in KAD15, is

$$H_\Sigma = NH_0. \quad (3.6)$$

In this paper, we generalize to cases in which  $N_+/N_-$  cells rotate clockwise/counter-clockwise and inject positive/negative helicity, with  $N_+ + N_- = N$ . The net helicity injected into the corona then becomes

$$H_\Sigma = (N_+ - N_-) H_0. \quad (3.7)$$

The case studied in KAD15 has  $N_+ = N$  and  $N_- = 0$ , so Equation (3.7) reduces to Equation (3.6). If, on the other hand,  $N_+ = N_-$ , equal numbers of cells rotate in each sense and the net injected helicity vanishes,  $H_\Sigma = 0$ . In our simulations described below, we allowed  $N_+$  and  $N_-$  to vary from cycle to cycle. The net helicity injected into the corona after  $M$  cycles therefore is

$$H_\Sigma = \sum_{i=1}^M (N_{+,i} - N_{-,i}) H_0, \quad (3.8)$$

where  $N_{+,i}/N_{-,i}$  is the number of cells that rotate clockwise/counter-clockwise during cycle  $i$ .

In each simulation, we assign a probability  $k$  that any individual top/bottom pair of cells injects positive helicity and  $1-k$  that the pair injects negative helicity. A random number  $\kappa_j \in [0, 1]$  is generated for each pair of cells  $j \in [1, N]$  during each cycle, and  $\kappa_j$  is compared with

$k$  to determine whether the sense of rotation is clockwise or counter-clockwise over that cycle. The helicity  $H_j$  injected by the  $j$ th pair of cells is

$$H_j = H_0 \times \begin{cases} +1 & \text{if } \kappa_j \leq k; \\ -1 & \text{if } \kappa_j > k. \end{cases} \quad (3.9)$$

On average, the expectation is that during each cycle, a fraction  $2k - 1$  of the maximum positive helicity  $NH_0$  will be injected into the corona,

$$\langle H_\Sigma \rangle = (2k - 1)NH_0 = fNH_0. \quad (3.10)$$

Throughout the paper, we will refer to  $k$  as the helicity preference of each simulation, and to  $f = 2k - 1$  as the net fractional helicity associated with  $k$ .

For this paper, the cases  $k = 0.75$  and  $k = 0.5$  were simulated to complement the  $k = 1$  case previously presented in KAD15. For reference, the expectation values of the net helicity injected per cycle are

$$\langle H_\Sigma \rangle = fNH_0 = NH_0 \times \begin{cases} 1.0 & \text{if } k = 1.0; \\ 0.5 & \text{if } k = 0.75; \\ 0.0 & \text{if } k = 0.5. \end{cases} \quad (3.11)$$

Below, we use the precise number of cells injecting each sign of helicity during each cycle to evaluate  $H_\Sigma$  in Equation (3.8). That prediction is compared to the instantaneous value  $H(t)$  calculated directly from the Finn & Antonsen (1985) volume integral for the relative magnetic helicity in the simulation, as described in KAD15.

The helicity preference  $k$  introduces one aspect of randomness into our simulations through the assignment of a clockwise/counter-clockwise sense of rotation (and positive/negative helicity) to each pair of rotation cells during each cycle of rotation. In order to emulate the stochastically shifting spatial pattern of convection on the solar surface and investigate its effect on coronal structure, we also introduce a second aspect of randomness into a separate set of simulations. After each cycle of rotations, we displace the entire hexagonal cellular pattern shown in Figure 2 by a randomly chosen angle  $\theta \in [0^\circ, 60^\circ]$  about its central vertical axis  $(y, z) = (0, 0)$ . For simplicity, the same angular displacement is applied to both the top and bottom plates, so that the top/bottom pairs of rotation cells remain aligned as before. Now, however, the random displacement means that the rotation cells will, in general, encompass parts of multiple neighboring flux tubes that were twisted during the previous cycle of rotations. The ensuing cycle therefore introduces braiding, as well as twisting, into the coronal magnetic field between the plates. As we will show, however, this displacement-induced braiding has no effect on the rate of helicity accumulation in the corona, and has only a minor influence on the smoothness of the induced magnetic structure. This result concurs with the qualitative conclusions of Zhao et al. (2015) from a much simpler simulation setup and is analyzed quantitatively here for the first time.

#### 4. RESULTS

In this section, we first describe the results of our simulations with both fixed and randomized patterns and for the various helicity preferences. Then, we analyze those results in the context of filament-channel formation and the smoothness of coronal loops.

#### 4.1. Fixed Cellular Pattern

The first set of simulations holds the cellular pattern fixed in the orientation shown in Figure 2, randomizing only the sense of rotation of the individual cells as described in §2. To compare the  $k = 0.75$  simulation most consistently with the  $k = 1.0$  case presented in KAD15, we ran it for twice as many cycles (42 vs. 21). As shown by Equation (3.8), the expectation value for the net injected helicity is the same (50% of  $42 \times N$  vs. 100% of  $21 \times N$ ). The  $k = 0.5$  case, in contrast, accumulates a net helicity only due to statistical fluctuations away from its average value of zero. For that case, therefore, we simply ran the simulation for 21 cycles. All three simulations then were extended for 5 additional cycles without imposing any rotational motions, to allow transients to die down and the system to relax toward a quasi-equilibrium final state.

As an example, Figure 3 shows the azimuthal component of the velocity on the bottom plate,  $V_\phi(x = 0, y, z)$ , during the first (left) and second (right) cycles of the  $k = 0.75$  case. For both the  $k = 0.75$  and  $k = 0.5$  cases, each individual cell does not necessarily preserve its sense of rotation from one cycle to the next. The sense of rotation is assigned randomly at each cycle, as given above in Equation (3.9). For  $k = 1.0$ , all cells rotate in the same sense in the first and second – indeed, throughout all – cycles.

Figure 4 shows the analytically expected (solid line) and numerically calculated (dashed line) helicities for each simulation. The orange ( $k = 1.0$ ) curve is the same as that presented in KAD15. After 21 cycles, the rotation cells have injected  $H = 36$  units of helicity. The red ( $k = 0.75$ ) curve shows that approximately the same  $H = 36$  units are injected over twice the time (cf. Equation 3.11) for the 75% preference. The blue ( $k = 0.5$ ) curve shows, as expected, that almost no net helicity is accumulated in the simulation with 50% preference over its first 21 cycles. All of the numerically calculated curves match very well the analytical values at each cycle, demonstrating that our simulations conserve helicity to a very high degree of accuracy. Therefore, the evolution of the magnetic field in our simulations is due predominantly to convection and reconnection, rather than to numerical diffusion that would dissipate helicity.

#### 4.2. Randomly Displaced Patterns

The second set of simulations is identical to the first, except that we also displace the entire hexagonal cellular pattern through a random angle after each cycle as described in §2. In these setups, different flux tubes wrap around each other, creating a braided field, in addition to being twisted by the rotation cells. We ran each simulation for the same number of cycles as in the fixed-pattern cases and for the same values of  $k$ .

As an example, Figure 5 shows  $V_\phi(x = 0, y, z)$  during the first (left) and second (right) cycles of the  $k = 0.75$  case. Like the corresponding fixed pattern cases, in the random  $k = 0.75$  and  $k = 0.5$  cases, each individual cell does not necessarily maintain its sense of rotation. Unlike the fixed pattern cases, however, the pattern itself is displaced by a random angle after each cycle. Except for the  $k = 1.0$  case, the randomized patterns (Fig. 5) exhibit different distributions of color than the fixed

patterns (Fig. 3). We used different sequences of random numbers  $\kappa_j$  to set the clockwise/counter-clockwise sense of rotation of the individual rotation cells in the two sets of simulations. The random angular displacements of the cellular pattern between the first and second cycles are evident by comparing the left and right columns for each helicity preference.

Figure 6 shows the analytically expected (solid line) and numerically calculated (dashed line) helicities for the various cases. Although the average helicities (Eq. 3.11) injected into the corona are identical for each value of  $k$ , the precise helicities (Eq. 3.8) actually injected differ between the fixed and randomized cases due to statistical fluctuations. Thus, the curves in Figures 4 and 6 are slightly different for  $k \neq 1.0$ . The orange ( $k = 1.0$ ) curve shows that the helicity injected for the 100% preference is identical for the fixed and randomized patterns, as expected. The red ( $k = 0.75$ ) curve shows that the 75% preference injects slightly more helicity in twice the time. The blue ( $k = 0.50$ ) curve shows that, as before, almost no net helicity is injected in this case. In this randomized-pattern simulation, the residual net helicity for the 50% preference is small and positive, whereas in the fixed-pattern simulation, it is negative. In all cases, we again find excellent agreement between the numerically calculated and analytically expected helicities.

#### 4.3. Formation of Filament Channels

Figure 7 shows the azimuthal component of the magnetic field in the horizontal mid-plane,  $B_\phi(x = 0.5, y, z)$ , halfway through the first cycle of twist for each simulation. At this early stage, each case exhibits the characteristic hexagonal pattern of rotation cells. For  $k = 1.0$ , every cell injects the same sign of  $B_\phi$ , so adjacent flux tubes always have oppositely directed twist fields and are able to reconnect readily. For the  $k = 0.75$  and  $k = 0.5$  cases, in contrast, adjacent twist fields sometimes are in the same direction. On average, this is true half the time in the  $k = 0.5$  case, suppressing reconnection between adjacent flux tubes whose twist fields are parallel rather than anti-parallel.

The effect of the helicity preference on the formation of filament channels can be seen clearly in the final-time  $B_\phi$  maps in Figure 8. The  $k = 1.0$  case has accumulated oppositely signed bands of twist flux at the outer and inner boundaries of the hexagonal pattern, as described previously in KAD15. These bands result from the inverse-cascade of twist flux from small to large scales due to reconnection, collecting at the boundaries to form filament channels according to the helicity-condensation model (Antiochos 2013). The  $k = 0.75$  case has been run out twice as long in order to accumulate roughly the same helicity, and it has acquired similar bands of twist at the outer and inner boundaries of the hexagonal pattern. Thus, despite the one-third (25%/75%) of twist fields on neighboring flux tubes that are parallel rather than anti-parallel in this simulation, sufficient reconnection has occurred to enable the helicity to condense at the flux-system boundaries here, as well. The shapes of the filament channels differ slightly in the  $k = 1.0$  and  $k = 0.75$  cases. The contrast is most evident in the randomized-pattern simulations, where the twist flux has a very uniform, circular appearance in the  $k = 1.0$  case, while the structure is more ragged, especially at

the inner boundary, in the  $k = 0.75$  case. At the largest scales, however, these two cases yield qualitatively identical outcomes: the twist flux forms two bands of opposite polarity at the boundaries of the hexagonal pattern of rotations. In the corona, such bands would manifest themselves as extended, sheared filament channels.

The sharply contrasting  $k = 0.5$  case, on the other hand, displays a very different final-time appearance. No long, coherent bands of twist flux have accumulated at either the outer or inner boundaries of the hexagonal pattern. Instead, there are localized concentrations of twist flux dispersed across the interior of the pattern, as well as at its boundaries. Because zero net helicity is injected into this system, on average, zero net twist flux is available to be transported by reconnection to the hexagonal boundaries where it can accumulate. Turning this argument around, if the net condensed twist flux were finite, then the net helicity would be finite as well. We demonstrated this result analytically in KAD15. Consequently, the helicity-condensation process does not form filament channels in the case of a 50% helicity preference.

These examples demonstrate that the helicity preference plays a major role in the organization of the twist flux and the formation of filament channels. The  $k = 0.75$  case forms similarly strong, although rather more structured, bands of twist flux over twice the time as the  $k = 1.0$  case. As is argued below, the time scale for filament-channel formation is inversely proportional to the average net fractional helicity injected, i.e. to  $f$ . This dependence is supported further by the absence of filament-channel structure in the  $k = 0.5$  case, whose predicted time scale for channel formation is infinite.

#### 4.4. Accumulation of Twist Flux

The results above demonstrate that there are major qualitative and quantitative contrasts between the results for different helicity preferences, but more minor differences between the fixed and random patterns for a given helicity preference. We begin the quantitative analysis of our simulations by calculating the positive twist flux  $\Phi_{tw}^+$  through the  $z = 0$  plane,

$$\Phi_{tw}^+ = \int_0^{L_x} dx \int_0^{L_y} dy B_{tw}^+(x, y, z = 0), \quad (4.1)$$

where the corresponding positive twist field  $B_{tw}^+$  is

$$B_{tw}^+ = \frac{1}{2}(B_\phi + |B_\phi|) \geq 0. \quad (4.2)$$

The twist flux  $\Phi_{tw}^+$  is plotted in Figure 9 for both the fixed (solid curves) and random (dashed curves) patterns. All six simulations exhibit a brief initial phase of ideal evolution, of about one rotation cycle in duration, in which twist flux is injected into and stored in individual, non-interacting flux tubes. At this stage, the sense of rotation of adjacent cells is irrelevant to the accumulation of twist flux. As the twisting continues, however, the flux tubes expand laterally to compress the volume between them. This forms and strengthens electric current sheets between neighboring tubes that have anti-parallel twist fields. Reconnection between such tubes commences during subsequent twist cycles. This process, together with the randomization of the sense of rotation of individual

cells (for  $k \neq 1.0$ ) and of the orientation of the cellular pattern (for the random cases), causes the curves to deviate increasingly from one another at later times.

The two cases with nonzero net fractional helicities,  $k = 1.0$  (orange) and  $k = 0.75$  (red), show relatively small differences between the fixed and random patterns for fixed  $k$ . Over the full duration of the simulations, each preference accumulates essentially the same twist flux. The slightly larger values for the  $k = 0.75$  case reflect the slightly larger magnetic helicities accumulated in those simulations (Figs. 4 and 6) compared to the  $k = 1.0$  case. All four of these simulations eventually accumulate twist flux at a rate per cycle that is in good agreement with the calculation by KAD15 (their Equation 4.13 and Figure 11),

$$\Delta\Phi_{tw} = \frac{1}{2} \frac{\Delta\langle H_\Sigma \rangle}{\Phi_N} = \frac{f}{2} \frac{H_0}{\Phi_0}, \quad (4.3)$$

where each of the  $N$  twisted flux tubes contains  $\Phi_0$  units of magnetic flux. The expression in Equation (4.3) assumes that the twist flux  $\Phi_{tw}$  condenses at the outer boundary of the flux system, which occurs in our simulations with  $k = 1.0$  and  $k = 0.75$ . In a spirit similar to KAD15 (their Equation 4.28), we calculate the filament-channel formation time  $\tau_{fc}$  over which a critical amount of twist magnetic flux  $\Delta\Phi_{fc}$  accumulates,

$$\tau_{fc} = \frac{\Delta\Phi_{fc}}{\Delta\Phi_{tw}} \tau_0 = \frac{2}{f} \left( \frac{\Phi_0}{H_0} \tau_0 \right) \Delta\Phi_{fc}, \quad (4.4)$$

where  $\tau_0$  is the duration of one twist cycle. Equations (4.3) and (4.4) quantitatively express the observed factor-of-two differences in twist-flux accumulation rates and filament-channel formation times between our  $k = 1.0$  ( $f = 1.0$ ) and  $k = 0.75$  ( $f = 0.5$ ) cases. They also predict how these quantities should change for other helicity preferences  $k$ .

Our last two simulations, with  $k = 0.5$ , have zero net fractional helicity,  $f = 0.0$ . For this case, the predicted accumulated twist flux  $\Delta\Phi_{tw}$  vanishes and the filament-channel formation time  $\tau_{fc}$  is infinite. We observe in these simulations (Figure 9) that the fluctuations in the twist flux are relatively large, and the average amount of flux saturates after about 10 cycles have elapsed. Thereafter, the average seems to be statistically quasi-steady, increasing or decreasing randomly according to the cycle-to-cycle variations of the sign of twist in individual rotation cells (in both simulations) and of the orientation of the cellular pattern (in the random-pattern simulation only). Evidently, these simulations have reached a roughly steady-state balance between the rates of twist-flux injection by the twisting motions and extraction via a combination of untwisting motions and reconnection between anti-parallel twist fields.

#### 4.5. Smoothness of Coronal Loops

We have seen that, when it is effective, the helicity-condensation process transports twist via reconnection to the boundaries of the flux system, where it condenses. This leaves the interior of the system relatively smooth and untwisted. The final configuration then corresponds to a corona with strong shear concentrated at its PILs and laminar coronal loops in interior regions away from its PILs. This result can be seen clearly in Figure 8. In

the  $k = 1.0$  and  $k = 0.75$  cases with nonzero net fractional helicities, at a glance, the interior of each flux system seems very smooth, with little twist evident. A careful comparison of the two cases reveals that the annular region between the filament channels is somewhat more structured for  $k = 0.75$ , with localized, small-amplitude twists of both signs accumulating in the interior. As might be anticipated, this structure is somewhat less noticeable for the simulations with randomly displaced patterns compared to their fixed-pattern counterparts.

The appearance of the  $k = 0.5$  is strikingly different from the  $k = 1.0$  and  $k = 0.75$  cases. For the fixed pattern especially (bottom row, left column of Figure 8), small-scale, coherent concentrations of twisted field are present throughout the interior of the hexagonal flow region. In addition, the magnitude of the accumulated twist is significantly smaller than in the  $k = 1.0$  and  $k = 0.75$  cases. This is due to both the random untwisting of previously twisted field lines in successive cycles and the zero net twist flux that can accumulate globally and be transported to the flux-system boundaries. The local twist concentrations that are formed appear and disappear transiently as the system evolves. Each such concentration has a lifetime on the order of one rotation period of the convection cells. Taking the rotation period to be of order a day, or the lifetime of a typical supergranule, these concentrations of twist should easily survive for timescales long enough to be detected remotely. The lack of such observations indicates that the photosphere likely injects helicity with a significant preference.

To demonstrate the stark difference in the amount of structure in the different helicity preference cases we plot in Fig. 10 a set of magnetic field lines from the same set of fixed points for the fixed-pattern  $k = 1$ ,  $k = 0.75$ , and  $k = 0.5$  cases. All of the field lines are chosen from the interior of the hexagonal region, which represents the ‘loop’ portion of the corona. The bottom plate represents magnetic field magnitude, which shows a structure similar to that shown in Fig. 8. Although only a sample of field lines is chosen, they are representative of the field lines in the rest of the ‘loop’ portion of the corona. The striking difference in the amount of structure in the corona is immediately evident by comparing the  $k = 1$  and  $k = 0.75$  cases with the  $k = 0.5$  case. In the latter simulation, field lines are twisted and braided around each other in a complicated fashion. In the first two cases, although the field lines are traced from the same points, the field lines themselves are quite smooth and laminar. There may appear to be some structure due to field lines passing behind, or in front of, each other, but there is almost no significant twisting or braiding around each other. In fact, the top two figures very closely resemble the initial, uniform field configuration, and, importantly, the smooth, laminar structure observed in Fig. 1, albeit in a plane-parallel geometry. In this sense, the  $k = 1$  and  $k = 0.75$  coronal loops are quasi-potential, while the  $k = 0.5$  coronal loops clearly deviate quite strongly from quasi-potentiality. In Fig. 11, a different set of field lines is plotted for the random-pattern  $k = 1$ ,  $k = 0.75$  and  $k = 0.5$  cases. These sample field lines are traced from the same footpoints in each case, and again demonstrate the quasi-potentiality of the corona in the former two cases, and the large amount of structure in the latter case.

#### 4.6. Fluctuations of Twist Field

To quantify the amount of small-scale structure in the various cases, we calculated the angle-averaged azimuthal magnetic field  $\langle B_\phi(r) \rangle$  and its root mean square deviation  $\delta B_\phi(r)$  in the mid plane ( $x = 0.5$ ). Specifically, we evaluated (for  $m = 1, 2$ )

$$\langle B_\phi^m(r) \rangle = \frac{1}{2\pi} \int_0^{2\pi} B_\phi^m(x = 0.5, y, z) d\phi, \quad (4.5)$$

$$\delta B_\phi(r) = \sqrt{\langle B_\phi^2(r) \rangle - \langle B_\phi(r) \rangle^2}, \quad (4.6)$$

where  $r = \sqrt{y^2 + z^2}$ . A discrete  $\rho$  grid, with the same spacing as the  $y$  and  $z$  grids, was adopted, and all cell-center positions  $(y, z)$  were grouped into corresponding  $r$  intervals to calculate the integrals in Equation (4.5). Figure 12 shows  $\delta B_\phi(r)$  at the end of the random pattern simulations for each value of  $k$  (color-coded). The rms deviations  $\delta B_\phi(r)$  shown in Figure 12 all exhibit small-scale statistical fluctuations. The average amplitude of the fluctuations is smallest for the 100% helicity preference ( $k = 1.0$ , orange) and largest for the 50% preference ( $k = 0.5$ , blue), where they are nearly three times as large compared to the 100% helicity preference. A very similar trend was seen in the fixed-pattern simulations. As evident from Figure 11, these localized fluctuations in twist field for the zero helicity case correspond to field line tangling that would easily be observed if it were present in the real corona.

#### 4.7. Length of Field Lines

Further insight into the overall magnetic structure of the corona is gleaned by examining the lengths of field lines throughout the domain. In Figure 13, we plot the length of magnetic field lines for the various helicity preferences. Here the differences between the filament channels and coronal loops is greatest in the  $k = 1.0$  simulations, where substantially longer field lines reside in the filament channels. The coronal loops in the interior are quite short. Indeed, their lengths are very close to those of the untwisted field lines exterior to the hexagonal region. The two  $k = 0.75$  simulations, meanwhile, display a slightly more mixed character in the interior. The coronal-loop field lines in these cases are slightly longer than the exterior untwisted field, although not nearly as long as the filament-channel field lines, which themselves are somewhat shorter than for  $k = 1.0$ .

As we found for several diagnostics described previously, the  $k = 0.5$  case displays a strikingly different appearance from those with nonzero net fractional helicities  $f$ . As can be seen in Figure 13 (bottom row), the hexagonal region of rotation cells hosts a rather homogeneous mixture of relatively short field lines, structured at small scales. This is not dissimilar to the interior of the hexagonal region in the  $k = 0.75$  case (middle row). However, no large-scale organization of the field-line length is evident, beyond the exclusion of twist from the center of the domain and the region beyond the perimeter of the hexagonal region. This is in sharp contrast to the cases  $k = 1.0$  and  $0.75$ , where much longer field lines accrue at both the inner and outer boundaries of the flux system.

### 5. IMPLICATIONS FOR CORONAL STRUCTURE

The results described in the preceding section have important implications for the global structure of the solar corona. Our findings demonstrate that the magnetic helicity preference  $k$  plays key roles in determining how the corona is structured and the time scale over which that structure develops. The contrast is particularly strong between the cases with 100% ( $k = 1.0$ ) and 50% ( $k = 0.5$ ) preferences and randomly displaced cellular patterns shown at the top and bottom right, respectively, in Figures 8 and 13. For the 100% preference, the twist flux condenses into two primary bands with opposite senses of twist at the inner and outer boundaries of the hexagonal region of rotation cells, with very little twist in the interior. These concentrations and dilution are reflected in the lengths of the associated magnetic field lines, which are very long near the two boundaries but minimally short in the interior. For the 50% preference, on the other hand, the twist flux does not condense into any recognizable global-scale structure, and the field lines have an essentially homogeneous distribution of intermediate lengths. These two cases have the largest and smallest (in magnitude) net fractional helicities,  $f = 1.0$  and  $f = 0.0$ , respectively.

Our intermediate case with 75% preference ( $k = 0.75$ ,  $f = 0.5$ ) exhibits some features of both of the previous limiting cases but, importantly, qualitatively resembles more closely the results for the 100% preference. The bands of condensed twist flux still form, albeit twice as slowly and with significant intrusions of twisted structures between them, and the field-line lengths are correspondingly longer at the hexagonal-region boundaries than in its interior, although with less contrast. Extrapolating to other cases with even smaller preferences but nonzero fractional helicities – say,  $k = 0.625$  and  $f = 0.25$  – we would expect these trends to continue, with a further increase in the filament-channel formation time (another doubling for  $f = 0.25$ ) and in the amount and homogeneity of small-scale structure in the interior of the hexagonal region.

Perhaps the clearest example of the effect of helicity preference on the structure of the closed loop corona is evident in Figures 10 and 11. The smoothness of the  $k = 1$  and  $k = 0.75$  coronal loops is manifestly different than the complexity of the  $k = 0.5$  coronal loops. Observations of the coronal magnetic field, meanwhile, invariably reveal smooth, laminar loops that closely resemble those observed in the  $k = 1$  and  $k = 0.75$  cases (cf. Figure 1), rather than those observed in the  $k = 0.5$  case. Our simulations indicate, therefore, that the photosphere must inject a significant net helicity so that structures such as those seen in the  $k = 0.5$  are not observed.

The simulation setups assumed in this paper are simplified compared to the complex photospheric polarity structure exhibited by the Sun, illustrated by Figure 1. Nevertheless, the quasi-random structure that we obtained for a 50% helicity preference, shown in the bottom panels of Figures 8 and 13, obviously does not resemble the clean, bimodal structure observed for the corona. In contrast, our results for both 100% and 75% preferences, shown in the other panels of those figures, do exhibit the bimodal characteristics of the corona: concentrations of twist at PILs in the form of highly nonpotential magnetic shear in filament channels, and generally smooth, quasi-potential fields free of twist away from PILs in ar-

chades of coronal loops. Therefore, a principal conclusion of our work is that the Sun must inject helicity into the corona with a significant hemispheric preference, favoring negative helicity forming left-handed structures in the north, and positive helicity forming right-handed structures in the south. These preferences are reflected in the observed statistics of solar filaments, sigmoids, and sunspot whorls. They also have been detected directly in the photospheric convection, although that measurement is very challenging, near the limits of observational resolution.

Our simulation is simplified in another important way compared to the Sun: there is no source of new, weakly sheared or unshaped magnetic flux in our domain, nor is there a sink of the strongly sheared flux condensing in the filament channels. Flux emergence from below the photosphere constantly injects fresh magnetic field into the corona, and coronal mass ejections regularly eject sheared magnetic field and its entrained magnetic helicity away from the Sun into the heliosphere. The characteristic time scales for these phenomena compete directly with the filament-channel formation time  $\tau_{fc}$  to establish a quasi-steady balance among these processes and the coronal magnetic structure that is observed. Such a calculation is well beyond the scope of this paper, but a first attack on the problem could be taken using global force-free modeling of the corona (e.g. Mackay et al. 2014). We point out that  $\tau_{fc}$  in Equation (4.4) is inversely proportional to the product of the net fractional helicity  $f$  and the angular rotation rate  $\omega_0$  of the twisting motions ( $H_0 \propto \omega_0 \tau_0$ ; KAD15). If this product  $f\omega_0$  is too small or too large, then the filament-channel formation time will be too long or too short compared to the emergence and ejection time scales, and the model is unlikely to replicate the Sun’s observed appearance. We anticipate that global modeling of the combined processes could provide rigorous bounds on the rotation rate  $\omega_0$ , to complement the narrowly constrained range of values available to the net fractional helicity,  $0.5 < f < 1.0$ .

Our simulations show that random displacements of the pattern of photospheric convection have only a secondary effect on the resulting coronal structure. This also is evident in Figures 8 and 13 by comparing the left (fixed-pattern) and right (random-pattern) columns for each helicity preference. The latter structures are somewhat smoother than the former, especially at small scales, but the large-scale organization is no different between them. This conclusion agrees with that reached by Zhao et al. (2015), who used a much simpler setup with far fewer rotation cells. The fundamental reason that the random convection pattern shows a very similar coronal end state to that of the fixed pattern is that, as shown by numerous simulations, magnetic reconnection is efficient at destroying all higher order topological features such as braiding, leaving only the global helicity (e.g., Wilmot-Smith et al. 2010). Our results are fully in agreement with this hypothesis.

In summary, this paper presents the first simulations of the evolution of the coronal magnetic field driven by photospheric motions with varying helicity preference. Our results agree well with the helicity condensation model of Antiochos (2013), which accounts for both the formation of sheared filament channels adjacent to PILs and the quasi-potential, smooth character of coronal loops

away from PILs. By transferring the magnetic twist injected by photospheric motions to ever larger scales, reconnection concentrates the twist at the boundaries of flux systems (i.e., at the PILs) while diluting it throughout their interiors. The remarkable implication of the model is that the global organization of the magnetic shear in the solar atmosphere is a direct consequence of local twisting of the footpoints of coronal flux tubes by surface convection. Even more remarkable and somewhat counter-intuitive, is our finding that in order for the hot closed corona – the loops – to exhibit no structure such as tangling or twisting, then a great deal of structure needs to be injected! The photospheric driving motions must have a clear helicity preference, in which case all the injected structure ends up localized around PILs. The corona, therefore, is a striking example on cosmic scales of a strongly self-organized system.

K.J.K acknowledges the use of post-processing codes originally written by Benjamin Lynch and Peter Wyper. K.J.K received funding for this work through a NASA Earth and Space Science Fellowship. The numerical simulations were performed under a grant of High-End Computing resources to C.R.D. at NASA’s Center for Climate Simulation. S.K.A. and C.R.D. were supported, in part, by grants from NASA’s Living With a Star and Heliophysics Supporting Research programs.

## REFERENCES

- Antiochos, S. K. 2013, *ApJ*, 772, 72  
 Attie, R., Innes, D. E., & Potts, H. E. 2009, *A&A*, 493, L13  
 Berger, M. A. 1984, *GApFD*, 30, 79  
 Bonet, J. A., Márquez, I., Sánchez Almeida, J., Cabello, I., & Domingo, V. 2008, *ApJ*, 687, L131  
 Bonet, J. A., Márquez, I., Sánchez Almeida, J., et al. 2010, *ApJ*, 723, L139  
 Brandt, P. N., Scharmer, G. B., Ferguson, S., Shine, R. A., & Tarbell, T. D. 1988, *Natur*, 335, 238  
 DeVore, C. R. 1991, *JCoPh*, 92, 142  
 DeVore, C. R., & Antiochos, S. K. 2008, *ApJ*, 680, 740  
 Duvall, Jr., T. L., & Gizon, L. 2000, *SoPh*, 192, 177  
 Finn, J., & Antonsen, T. 1985, *CoPPC*, 9, 111  
 Gaizauskas, V. 2000, in *Encyclopedia of Astronomy and Astrophysics*, ed. P. Murdin (Bristol: IOP), 2278  
 Gizon, L., & Duvall, Jr., T. L. 2003, in *ESA Special Publication, Vol. 517, GONG+ 2002 Local and Global Helioseismology: the Present and Future*, ed. H. Sawaya-Lacoste (Noordwijk: ESA), 43  
 Hagino, M., & Sakurai, T. 2002, in *Multi-Wavelength Observations of Coronal Structure and Dynamics*, ed. P. C. H. Martens & D. Cauffman (Pergamon: Amsterdam), 147  
 Hale, G. E. 1927, *Nature*, 119, 708  
 Hirzberger, J., Gizon, L., Solanki, S. K., & Duvall, T. L. 2008, *SoPh*, 251, 417  
 Knizhnik, K. J., Antiochos, S. K., & DeVore, C. R. 2015, *ApJ*, 809, 137  
 Komm, R., Howe, R., Hill, F., et al. 2007, *ApJ*, 667, 571  
 Liu, Y., & Schuck, P. W. 2012, *ApJ*, 761, 105  
 Mackay, D. H., DeVore, C. R., & Antiochos, S. K. 2014, *ApJ*, 784, 164  
 Martin, S. F. 1994, in *ASP Conf. Ser., Vol. 68, Solar Active Region Evolution: Comparing Models with Observations*, ed. K. S. Balasubramaniam & G. W. Simon (San Francisco: ASP), 264  
 Martin, S. F. 1998, *SoPh*, 182, 107  
 Martin, S. F., Marquette, W. H., & Bilimoria, R. 1992, in *ASP Conf. Ser., Vol. 27, The Solar Cycle*, ed. K. L. Harvey (San Francisco: ASP), 53  
 Parker, E. N. 1972, *ApJ*, 174, 499  
 Pevtsov, A. A., Balasubramaniam, K. S., & Rogers, J. W. 2003, *ApJ*, 595, 500  
 Pevtsov, A. A., Berger, M. A., Nindos, A., Norton, A. A., & van Driel-Gesztelyi, L. 2014, *SSRv*, 186, 285  
 Pevtsov, A. A., & Longcope, D. W. 2001, in *ASP Conf. Ser., Vol. 236, Advanced Solar Polarimetry – Theory, Observation, and Instrumentation*, ed. M. Sigwarth (San Francisco: ASP), 423  
 Rappazzo, A. F., Velli, M., & Einaudi, G. 2013, *ApJ*, 771, 76  
 Rust, D. M., & Kumar, A. 1994, *SoPh*, 155, 69  
 —. 1996, *ApJ*, 464, L199  
 Schmieder, B., Roudier, T., Mein, N., et al. 2014, *A&A*, 564, A104  
 Schrijver, C. J., Title, A. M., Berger, T. E., et al. 1999, *SoPh*, 187, 261  
 Seehafer, N. 1990, *SoPh*, 125, 219  
 Seligman, D., Petrie, G. J. D., & Komm, R. 2014, *ApJ*, 795, 113  
 Taylor, J. B. 1974, *PhRvL*, 33, 1139  
 —. 1986, *RvMP*, 58, 741  
 Vargas Domínguez, S., Palacios, J., Balmaceda, L., Cabello, I., & Domingo, V. 2011, *MNRAS*, 416, 148  
 —. 2015, *SoPh*, 290, 301  
 Wilmot-Smith, A. L., Pontin, D. I., & Hornig, G. 2010, *A&A*, 516, A5  
 Woltjer, L. 1958, *PNAS*, 44, 489  
 Zhao, L., DeVore, C. R., Antiochos, S. K., & Zurbuchen, T. H. 2015, *ApJ*, 805, 61  
 Zirker, J. B., Martin, S. F., Harvey, K., & Gaizauskas, V. 1997, *SoPh*, 175, 27

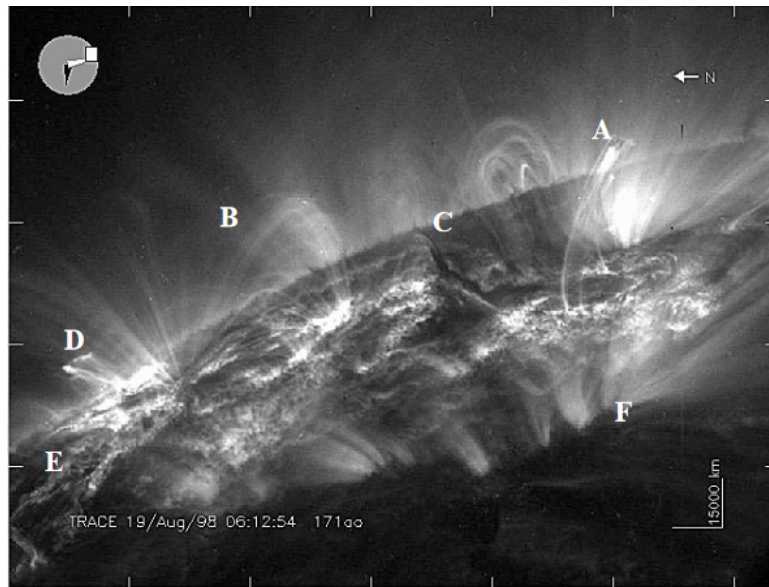


**Figure 1.** Coronal loops as observed by TRACE, showing their quasi-potential structure, with little to no tangling. (From Schrijver et al. 1999)

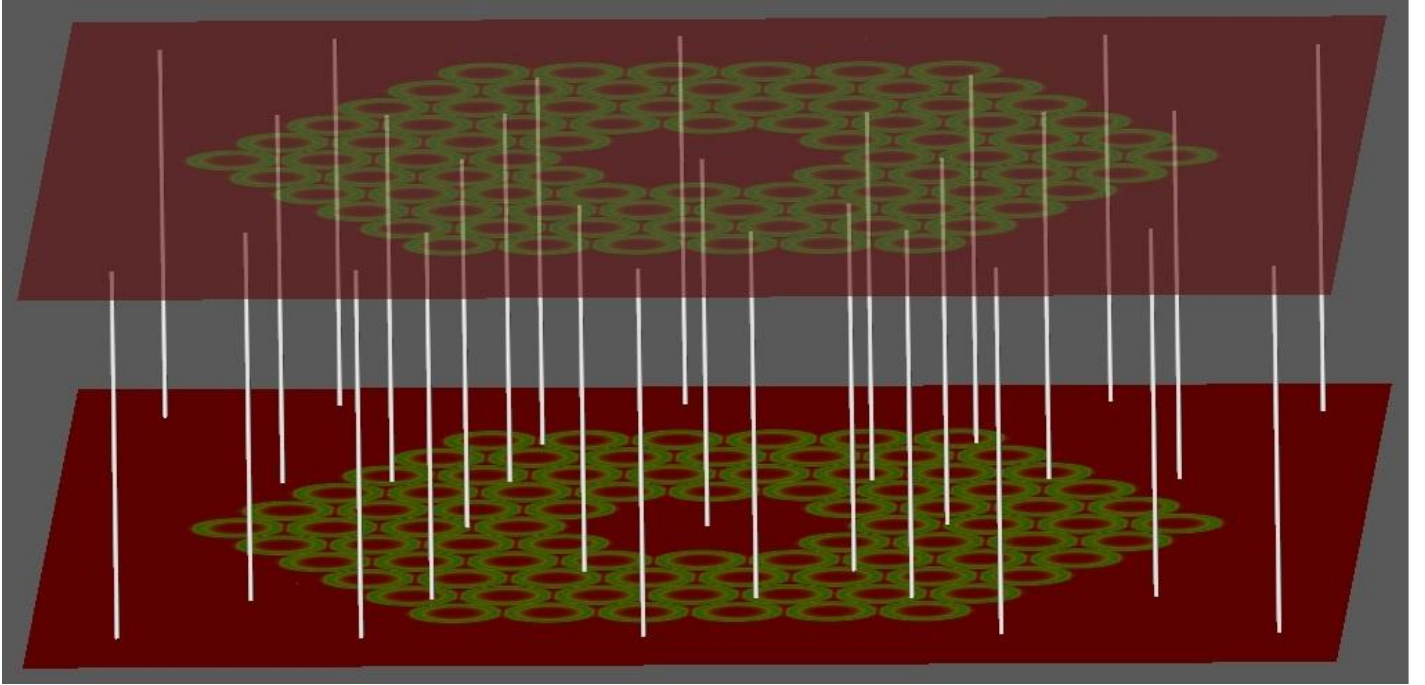


**Figure 2.** Setup of the numerical simulations. White lines represent the initial vertical magnetic field; color shading on the top and bottom plates represents velocity magnitude. To emulate the random photospheric convection in our numerical experiments, the local sense of rotation (clockwise/counter-clockwise) of individual convective cells shown in this figure can be set randomly, and the global hexagonal pattern of the cells collectively can be rotated randomly about its center. See text for details.

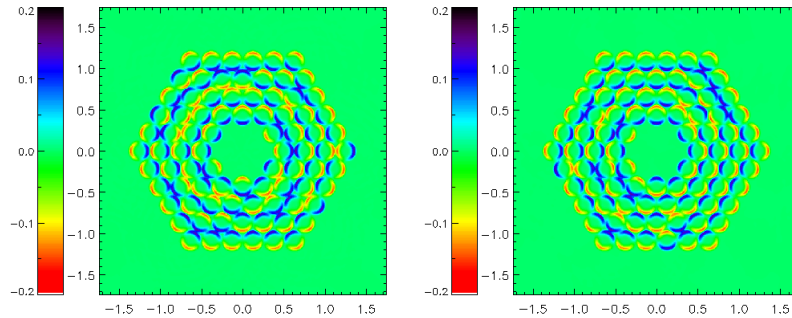


**Figure 3.**  $V_\phi$  on the bottom plate for the fixed-pattern case with  $k = 0.75$  during the first (left) and second (right) cycles.

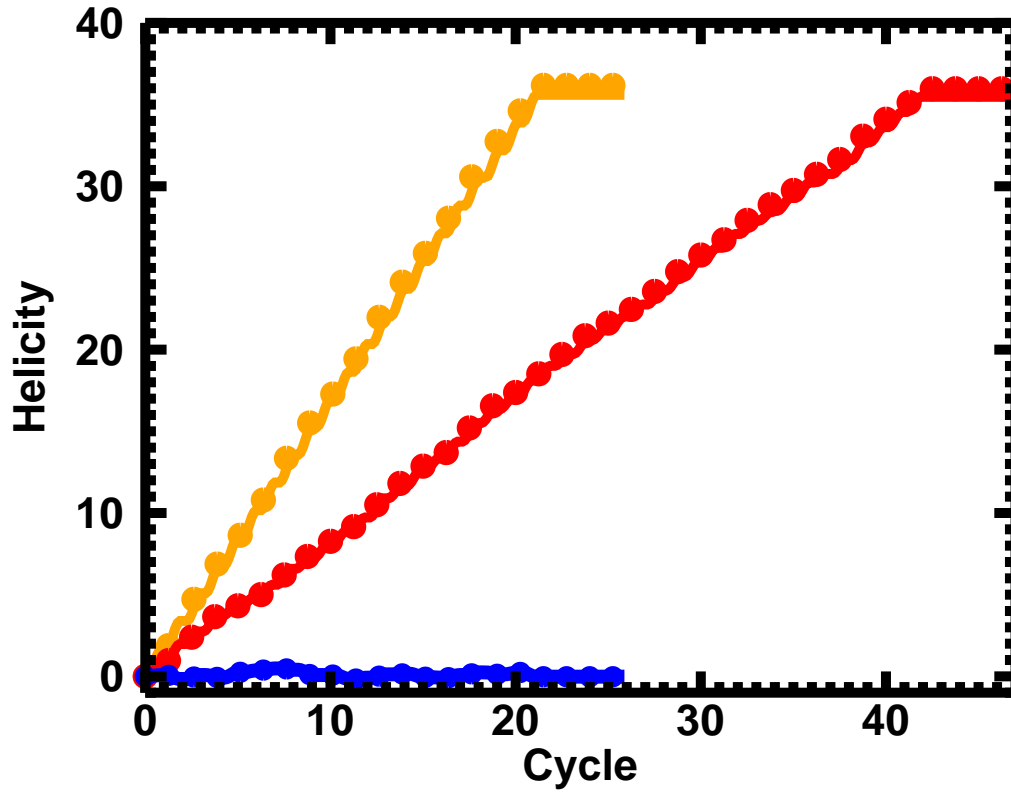


**Figure 4.** Helicity for fixed-pattern simulations. Solid curves are the analytically expected helicity based on the number of convective cells injecting positive and negative helicity during each cycle; filled circles are the numerically calculated values. The orange, red, and blue curves represent the  $k = 1$ ,  $k = 0.75$ , and  $k = 0.5$  cases, respectively.

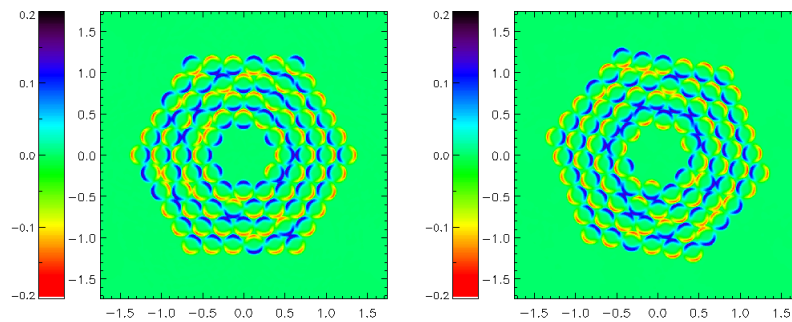


**Figure 5.**  $V_\phi$  on the bottom plate for the random-pattern case with  $k = 0.75$  during the first (left) and second (right) cycles.

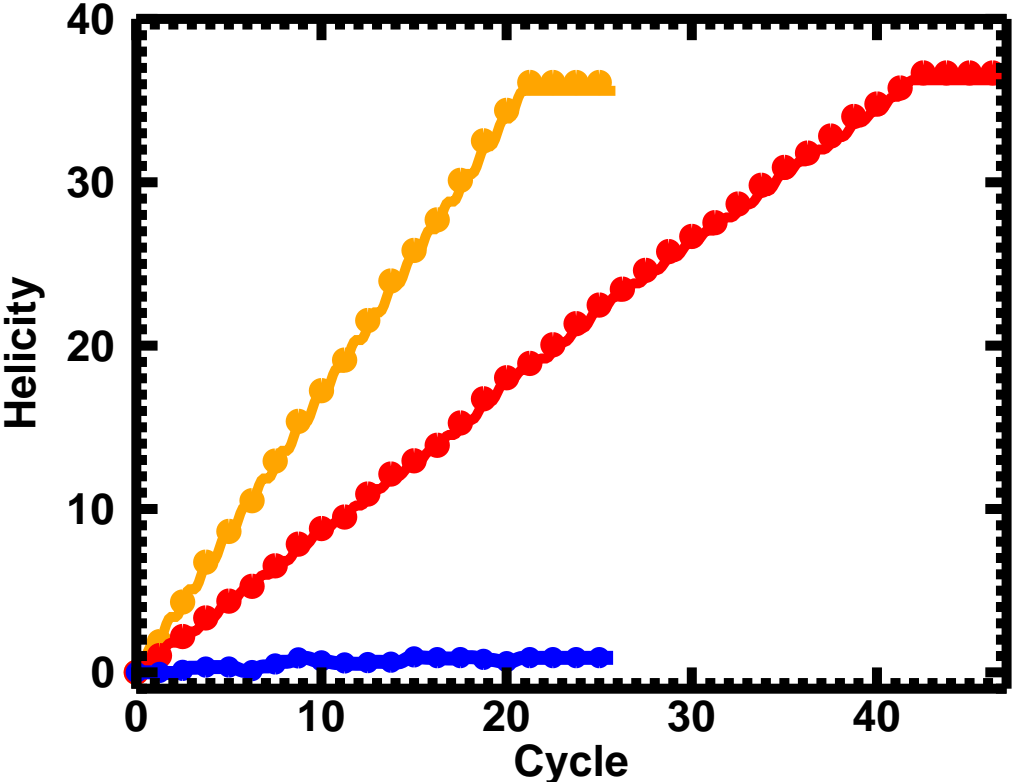


**Figure 6.** Helicity for random-pattern simulations. Solid curves are the analytically expected helicity based on the number of convective cells injecting positive and negative helicity during each cycle; filled circles are the numerically calculated values. The orange, red, and blue curves represent the  $k = 1$ ,  $k = 0.75$ , and  $k = 0.5$  cases, respectively.

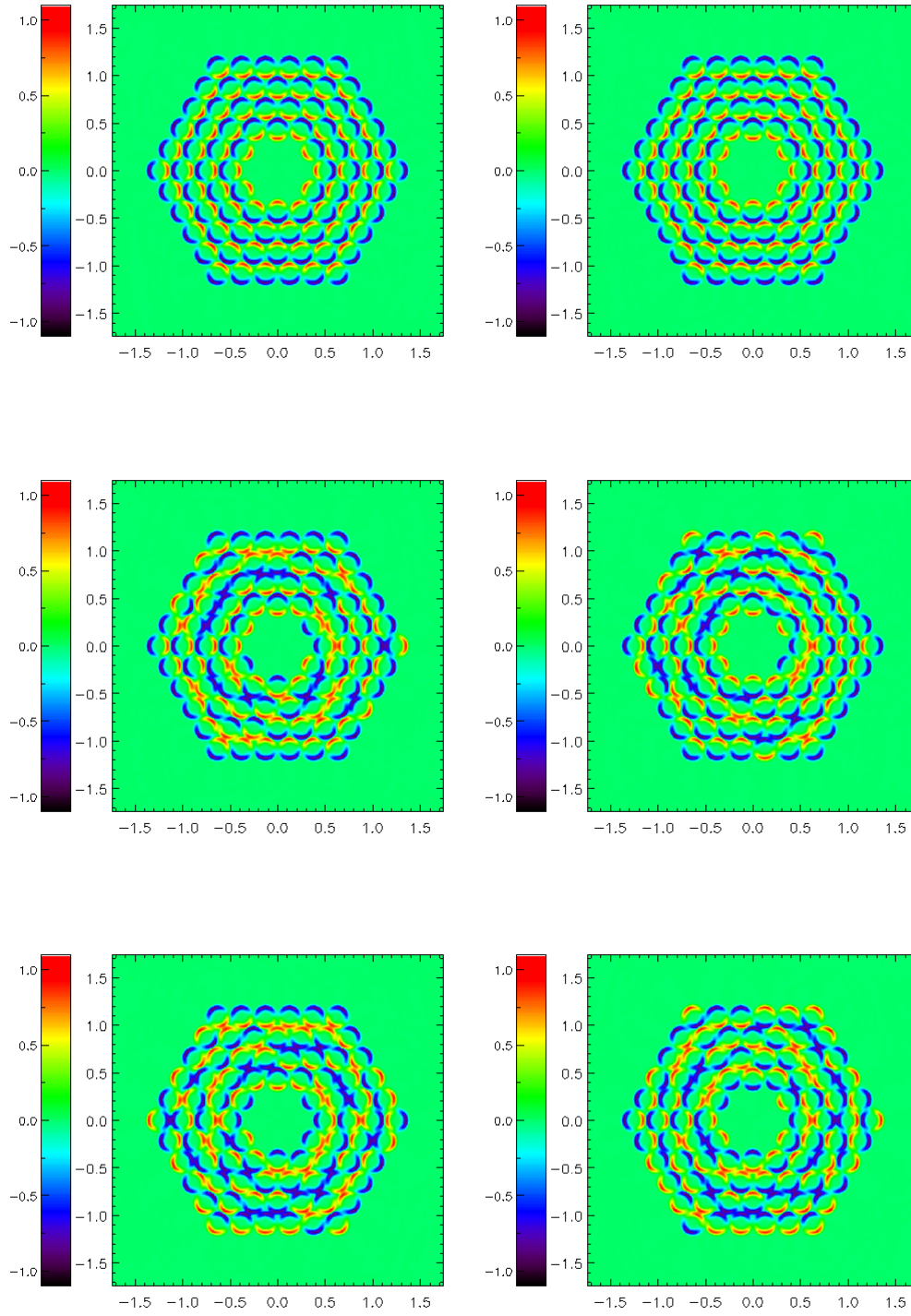


**Figure 7.** Twist field  $B_\phi$  (color shading) in the mid-plane ( $x = 0.5$ ) halfway through the first cycle of the fixed-pattern (left) and random-pattern (right) simulations. From top to bottom are the  $k = 1$ ,  $k = 0.75$ , and  $k = 0.5$  cases, respectively. Red/yellow (blue/teal) represents clockwise (counter-clockwise) twist.

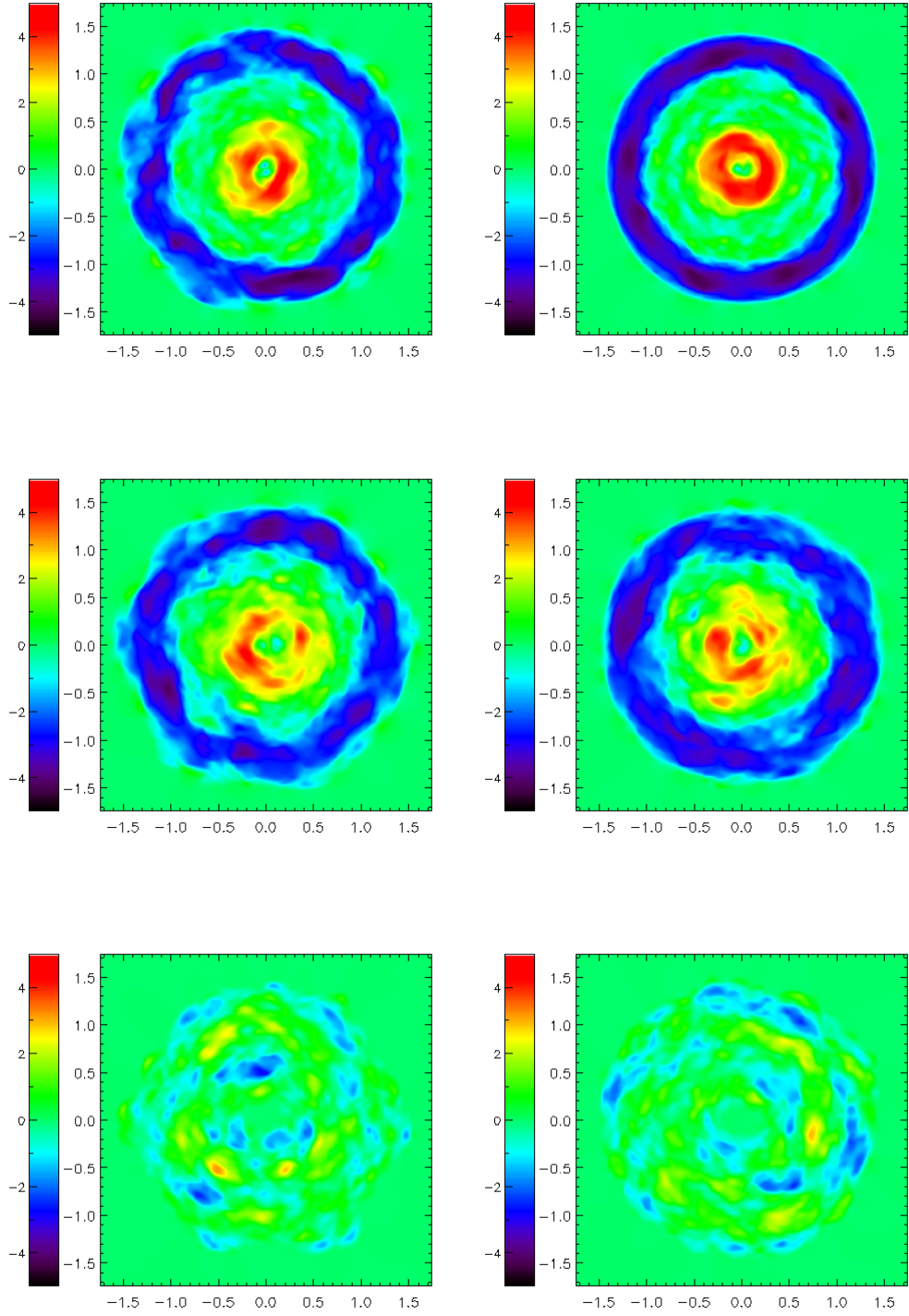


**Figure 8.** Twist field  $B_\phi$  (color shading) in the mid-plane ( $x = 0.5$ ) at the end of the fixed-pattern (left) and random-pattern (right) simulations. From top to bottom are the  $k = 1$ ,  $k = 0.75$ , and  $k = 0.5$  cases, respectively. Red/yellow (blue/teal) represents clockwise (counter-clockwise) twist.

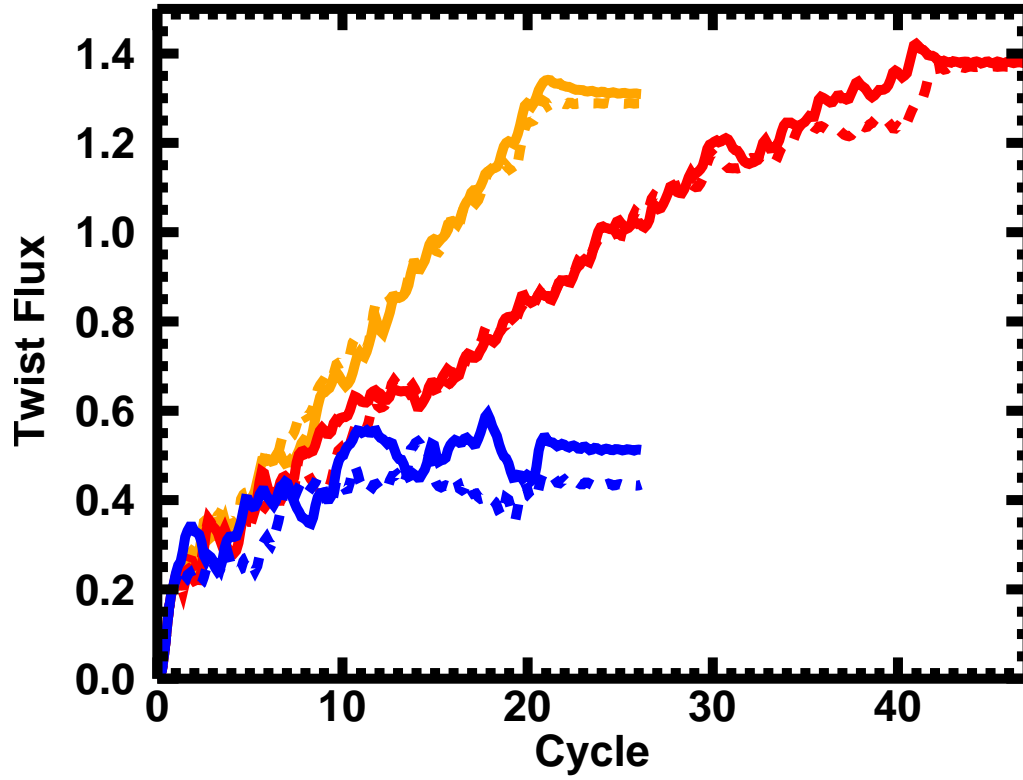


**Figure 9.** Positive twist flux  $\Phi_{tw}^+$  versus cycle through the vertical half-plane  $z = 0$  for the fixed-pattern (solid curves) and random-pattern (dashed curves) cases with  $k = 1$  (orange),  $k = 0.75$  (red), and  $k = 0.5$  (blue).

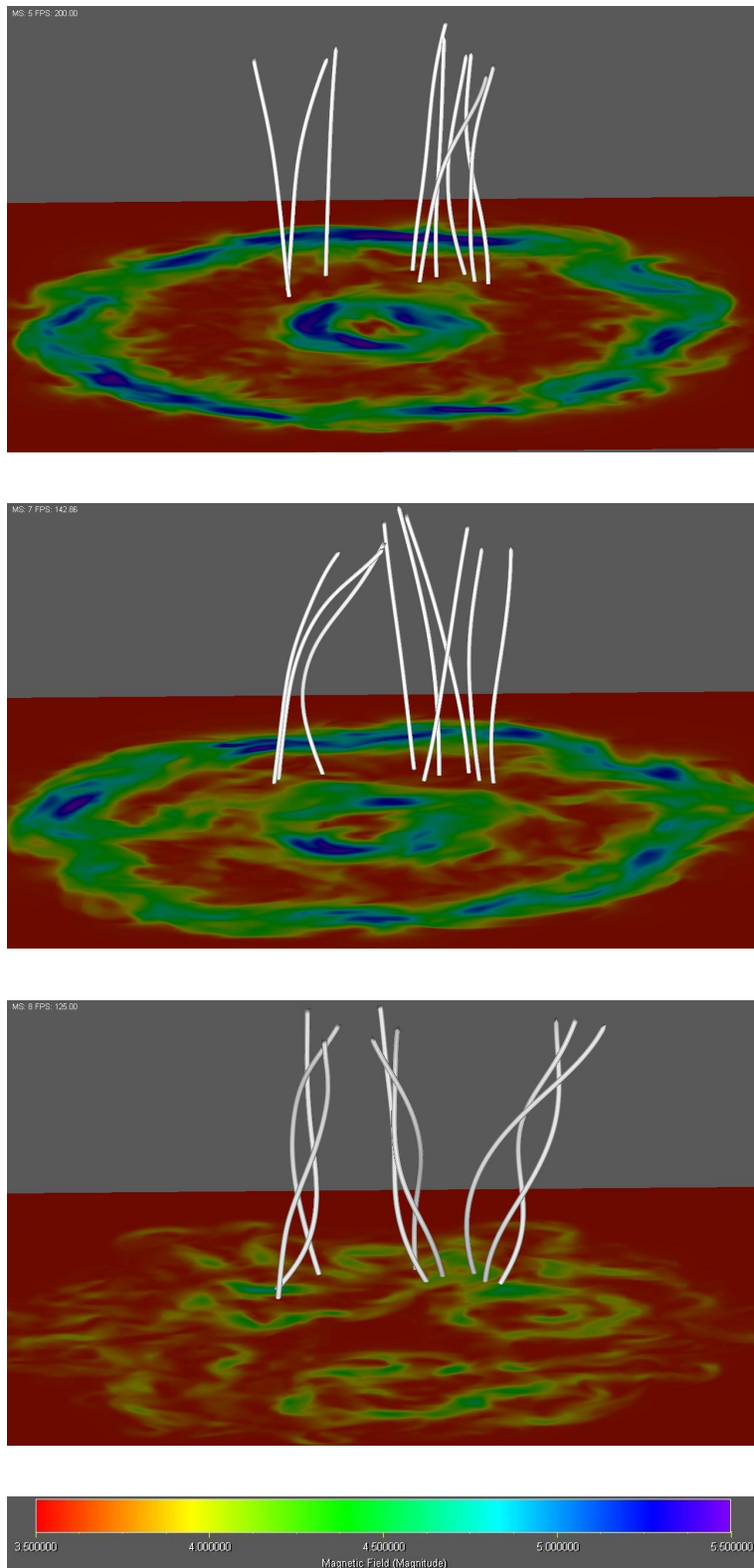


**Figure 10.** A sample of ‘coronal loop’ field lines (white) plotted at the end of the fixed-pattern  $k = 1$  (top)  $k = 0.75$  (middle) and  $k = 0.5$  (bottom) simulations. The field lines are plotted inside the interior of the hexagonal region on the bottom plate, which shows magnetic field magnitude (color shading). The initial (potential) field is a uniform straight field.

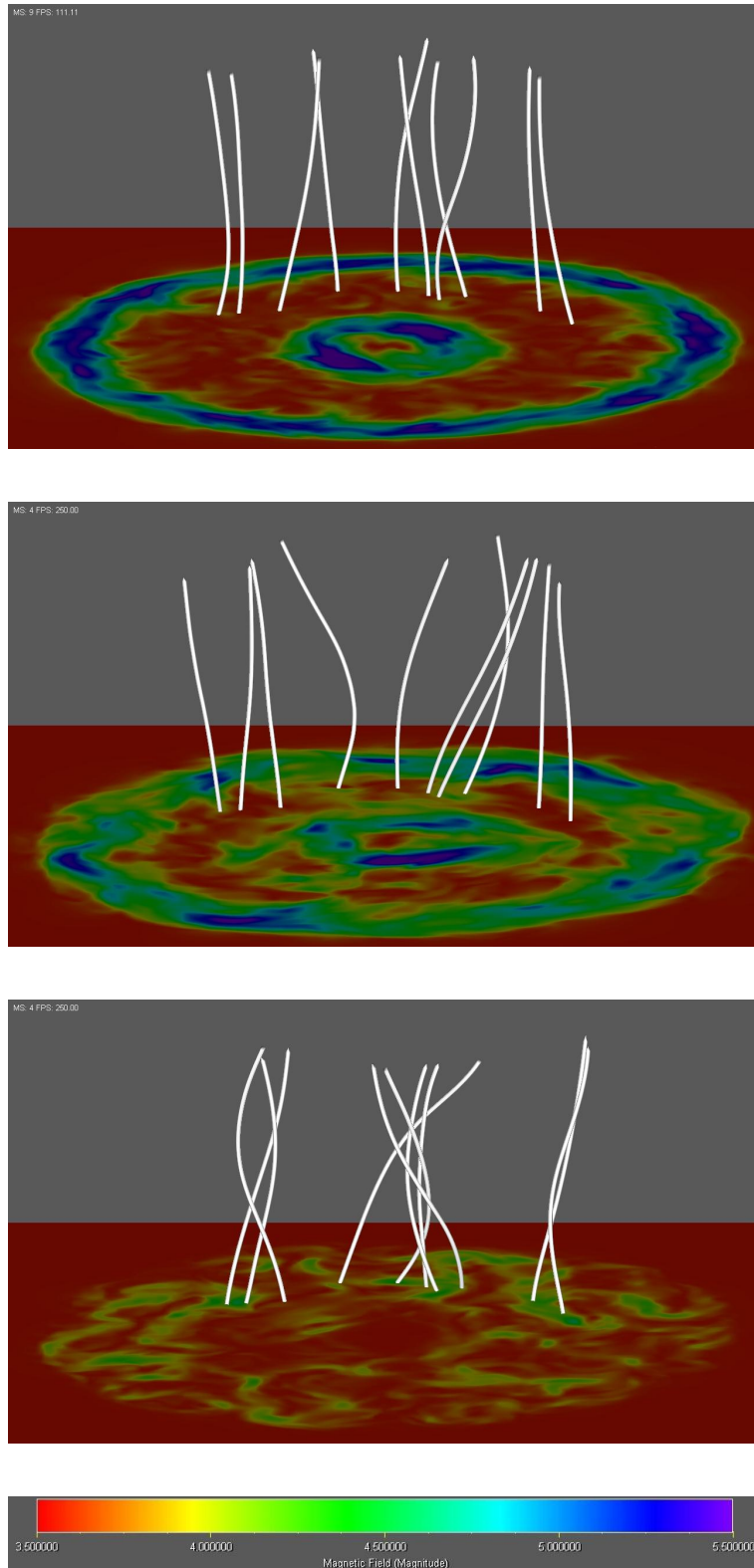


**Figure 11.** A sample of ‘coronal loop’ field lines (white) plotted at the end of the random-pattern  $k = 1$  (top)  $k = 0.75$  (middle) and  $k = 0.5$  (bottom) simulations. The field lines are plotted inside the interior of the hexagonal region on the bottom plate, which shows magnetic field magnitude (color shading). The initial (potential) field is a uniform straight field.

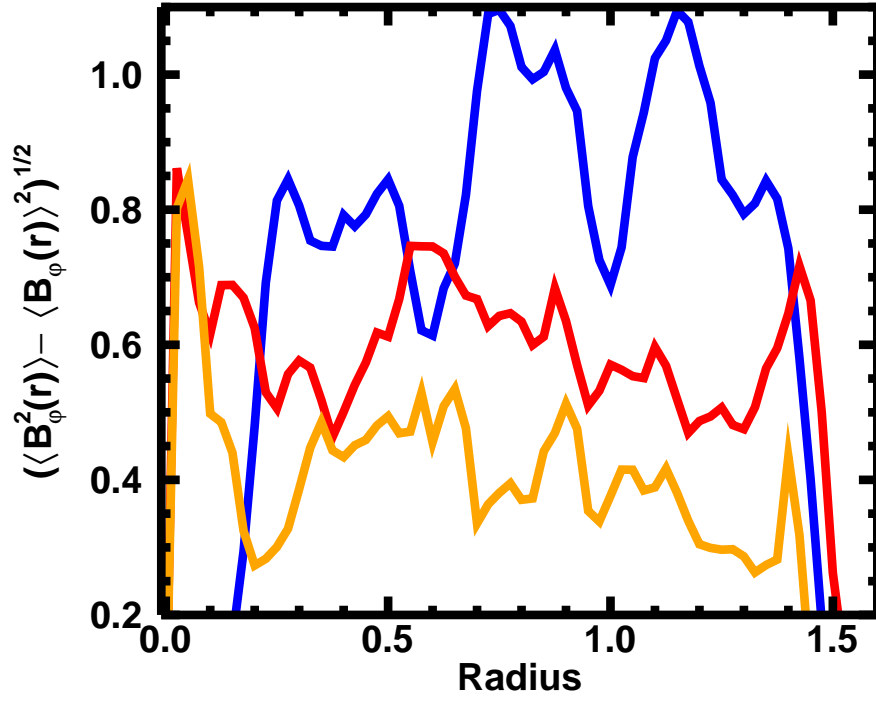


**Figure 12.** Root mean square deviation of azimuthal magnetic field  $\delta B_\phi(r)$  versus radius in the mid-plane ( $x = 0.5$ ) at the end of the random-pattern case with  $k = 1$  (orange),  $k = 0.75$  (red), and  $k = 0.5$  (blue).

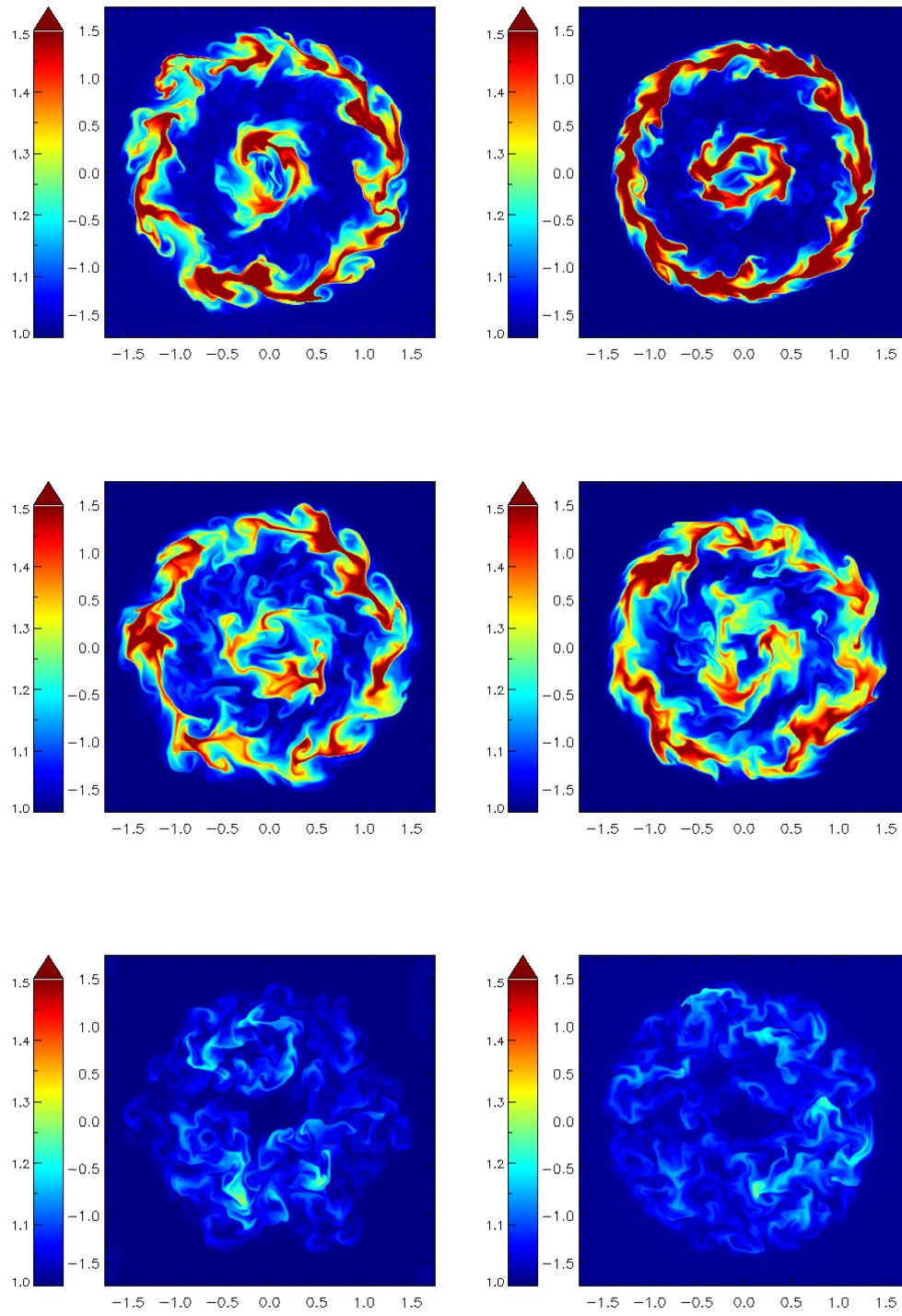


**Figure 13.** Maps of field line length at the end of the fixed-pattern (left) and random-pattern (right) cases with  $k = 1$  (top row),  $k = 0.75$  (middle row), and  $k = 0.5$  (bottom row).